On the Reversibility of Oxygen Incorporation in Metastable Bixbyite V_2O_3 Nanocrystals

Amy Bergerud[1,2,3], Sverre M. Selbach[3], and Delia J. Milliron[2]*

[1)] Department of Materials Science and Engineering, University of California, Berkeley, California, USA

[2)] McKetta Department of Chemical Engineering, The University of Texas at Austin, Austin, Texas, USA

[3)] Department of Materials Science and Engineering, Norwegian University of Science and Technology, Trondheim, Norway

ABSTRACT

A new, metastable polymorph of V_2O_3 with a bixbyite structure was recently stabilized in colloidal nanocrystal form. Here, we report the reversible incorporation of oxygen in this material, which can be controlled by varying temperature and oxygen partial pressure. Based on X-ray diffraction (XRD) and thermogravimetric analysis, we find that oxygen occupies interstitials sites in the bixbyite lattice. Two oxygen atoms per unit cell can be incorporated rapidly and with minimal changes to the structure, while the addition of three or more oxygen atoms destabilizes the structure, resulting in a phase change that can be reversed upon oxygen removal. Density functional theory (DFT) supports the reversible occupation of interstitial sites in bixbyite by oxygen and the 1.1 eV barrier to oxygen diffusion predicted by DFT matches the activation energy of the oxidation process derived from observations by *in situ* XRD. Thus, the observed rapid oxidation kinetics are facilitated by short diffusion paths through the bixbyite nanocrystals. Due to the exceptionally low temperatures of oxidation and reduction, this earth-abundant material is proposed for use in oxygen storage applications.

The oxides of vanadium are known for both their structural complexity and fascinating properties, as manifested in the many stable and metastable phases and phase transitions that exist in these materials. Vanadium sesquioxide (V_2O_3) is one such oxide, transforming from the antiferromagnetic, insulating monoclinic phase to the paramagnetic, metallic corundum phase at 170 K.[1–3] This phase transformation is of great fundamental importance due to its model Mott-Hubbard transition behavior.[4] Recently, a metastable phase of V_2O_3 with a cubic, bixbyite structure was discovered.[5] This new polymorph has since been the subject of several studies, both fundamental and applied, including its proposed use as a p-type conductor and battery electrode.[6,7] Synthesizing V_2O_3 nanocrystals stabilizes the metastable phase and allowed us, in 2013, to prepare phase pure bixbyite.[8] Using our colloidal synthetic method, we now demonstrate low temperature, reversible oxidation and reduction of bixbyite V_2O_3 nanocrystals, a phenomenon which could be harnessed for oxygen storage.

The bixbyite structure has a body-centered cubic lattice with space group *Ia*-3. Often described as anion deficient fluorite, bixbyite is comparable to a 2 x 2 x 2 fluorite supercell with a quarter of the anions removed, as demonstrated in **Figure 1**. These vacated sites are the 16c Wyckoff positions in the *Ia*-3 space group, which are inherently unfilled in bixbyite.[9] Cations in the bixbyite structure populate two symmetry inequivalent positions- the 8b and 24d Wyckoff positions, otherwise known as b- and d-sites,

while anions populate the 48e positions for a total of 80 atoms in the unit cell. Bixbyite is the stable polymorph of several M_2O_3 type oxides, including indium oxide, yttrium oxide, and manganese oxide. As a vanadium oxide, this phase was found to be metastable, transforming to the bulk stable corundum phase of V_2O_3 upon heating in an inert atmosphere. Since the initial discovery of bixbyite V_2O_3, several papers have been published on the subject, but only three synthetic routes to the bixbyite polymorph have been reported as of yet. Weber et al. synthesized a mixture of corundum and bixbyite V_2O_3 from the reduction of vanadium trifluoride at 600°C in water saturated forming gas.[5] This mixture was observed to transform to pure corundum phase upon heating to 550°C in argon. Xu et al. formed bixbyite with an urchin-like morphology through the thermal decomposition of vanadyl ethylene glycolate.[7] Transformation to corundum occurred upon heating in argon at 540°C in this instance. Lastly, we previously reported a colloidal route to bixbyite nanocrystals (NCs) with enhanced stability relative to its bulk counterparts.[8] Transformation to corundum proceeded slowly over the course of about 1 hour when held at 700°C, and was accompanied by particle coarsening. This enhanced stability was reasoned to be due to the non-negligible effect of surface energy on Gibbs free energy at the nanoscale, a well-known phenomenon in nanocrystals.[10–12] The suspected lower surface energy of bixbyite is thought to alter the relative energetics of the two phases, potentially favoring bixbyite over corundum below some critical size.

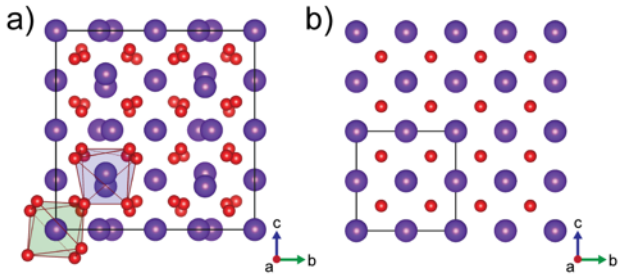

Figure 1. a) Bixbyite unit cell with b- and d- sites marked with green and blue polyhedra, respectively. b) The undistorted fluorite structure is shown for comparison. Cations are colored purple and anions are red, while black lines mark the border of the unit cell in each structure. All crystal structure figures were created using VESTA.[13]

In addition to experimental reports, several theoretical studies on bixbyite V_2O_3 have been published in recent years, including calculations of electronic and magnetic properties, intrinsic and extrinsic defects, and phase stabilities. Using GGA+U and hybrid density functional theory (DFT) calculations, Wessel et al. compared the energetics of the known polymorphs of V_2O_3 along with other defective fluorite-type structures, confirming the metastable nature of the bixbyite polymorph.[14] Antiferromagnetic ordering minimized the energy of the system and led to the formation of a band gap, both of which were confirmed by previous experimental work by the same group.[5] Sarmadian et al. recently published a detailed study on p-type dopants in bixbyite.[6] Using a hybrid HSE06 functional, magnesium was found to be a shallow acceptor and therefore Mg-doped bixbyite is theorized to be a p-type conductor. Vanadium vacancies were also found to be shallow acceptors and may also result in p-type conductivity. To understand the very low oxygen partial pressures required to stabilize the bixbyite phase in ref. 5, Reimann et al. also used DFT, with both GGA and hybrid functionals, to study intrinsic defects in bixbyite.[15] The formation of oxygen interstitials in the 16c Wyckoff position was found to be favorable

under ambient conditions, and an oxygen partial pressure of 10^{-17} bar was estimated to be required to thermodynamically favor the formation of stoichiometric bixbyite under their reaction conditions.

In our previous publication, we noted a change in crystal structure of bixbyite V_2O_3 nanocrystals upon air exposure, thought to be due to oxidation.[8] Here, we explore the oxidation of bixbyite nanocrystals in detail, using *in situ* x-ray diffraction (XRD) to observe structural changes in real time and complementing the experimental findings with DFT calculations. The oxidation process is found to be reversible upon heating in inert atmosphere at moderate temperatures (>325°C), thereby establishing the possibility for use in low-temperature oxygen storage applications, where oxygen is reversibly stored and released, e.g. for gas separation or to carry out catalytic processes.[16–18]

RESULTS

Upon exposure to air, the crystal structure of the bixbyite nanocrystals changes gradually over the course of weeks at room temperature, as observed by XRD. The change is accelerated at higher temperatures, occurring over the course of approximately an hour at 125°C, eventually resulting in a phase transformation to an unknown phase of vanadium oxide with no obvious changes in particle shape and size (**Figure 2a & b, Figure S1**). Before this transformation occurs, XRD peaks shift to lower Q values while some peaks decrease in intensity, suggesting lattice expansion and changes in atomic positions, respectively. This evolution is shown for samples heated in air at 125°C, by both *ex situ* and *in situ* XRD*,* in **Figure 2c, d, & e**. To support this interpretation, Rietveld refinement was performed on XRD scans of bixbyite NCs annealed in air at 125°C for 0, 10, 20, 30, and 40 minutes (**Figure S2**). These results, shown in **Figure 2f,** confirm that the cubic lattice parameter increases while vanadium located in the 24d Wyckoff positions in bixbyite shift location within the unit cell with increasing annealing time. This shift in vanadium position can also be described as the structure becoming more “fluorite-like,” an indication that the vacant 16c Wyckoff positions may be filled by oxygen interstitials during the process. Thermogravimetric analysis (TGA) also shows an increase in weight when bixbyite is heated in air yielding further confirmation of oxygen insertion into the bixbyite lattice.[8]

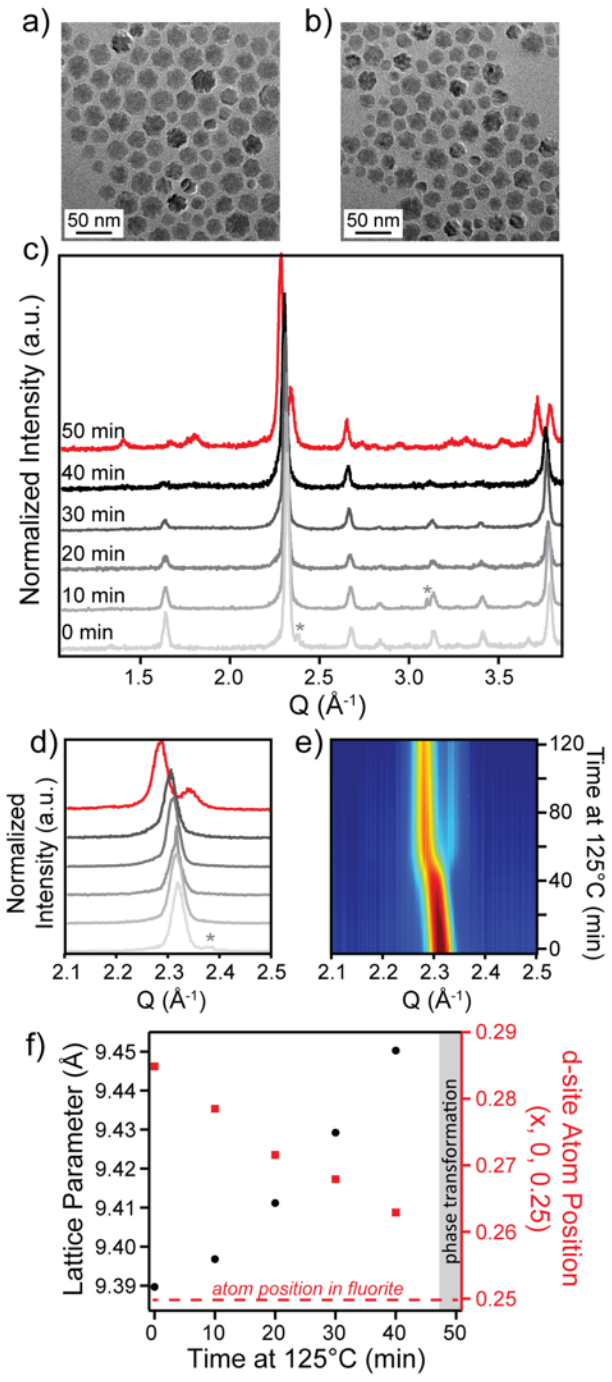

Figure 2- Transmission electron microscopy images of bixbyite NCs a) as synthesized and b) after annealing at 125°C in air for 2 hours. c) XRD scans of bixbyite annealed in air at 125°C for 0, 10, 20, 30, 40, and 50 minutes (with impurity peaks from the Si substrate marked with *) with d) a zoomed in image of the (222) peak, e) *in situ* XRD pattern centered at the (222) bixbyite peak held at 125°C in air, and f) results of Rietveld refinement for films annealed at 125°C for 0, 10, 20, 30, and 40 minutes showing lattice parameter (left/black) and position of the d-site vanadium (right/red) as a function of annealing time.

Static DFT calculations were used to map the energy landscape of the likely interstitial oxygen positions in the bixbyite unit cell. The total energy of the system upon moving one interstitial oxygen along channels parallel to the edge, face diagonal, and body diagonal of the bixbyite unit cell was calculated and the results are shown in **Figure 3**. Since test calculations revealed that the trends in interstitial oxygen position were insensitive to magnetic order and spin polarization (**Figure S9**), these parameters were not included in the calcuations to reduce computational cost.

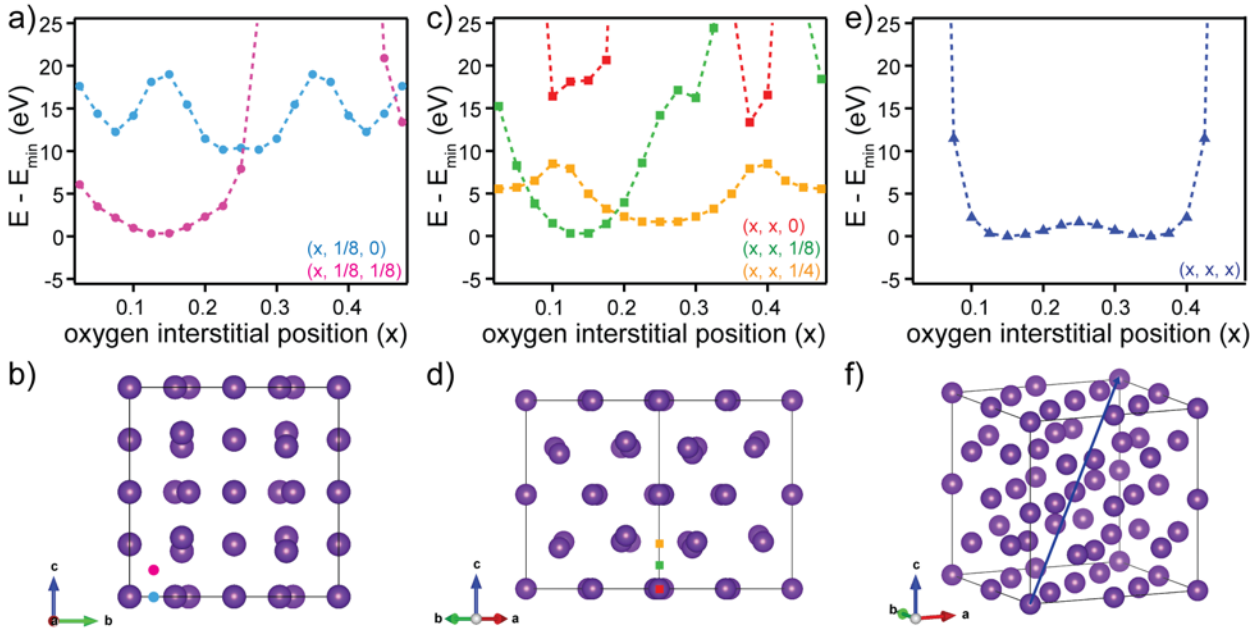

Figure 3- Energy of the bixbyite unit cell with an oxygen interstitial placed along channels parallel to the a) cube edge, c) face diagonal, and e) body diagonal, referenced to minimum energy value. Channels marked in structures below (b, d, f). Positions are indicated in terms of fractional coordinates in the cubic unit cell.

As expected, and previously assumed without energy mapping in other work, the most stable positions for oxygen interstitials are the inherently vacant 16c Wyckoff positions in the *Ia*-3 space group.[15] This is evident from the minima found at the fractional coordinates (0.15, 0.15, 0.15) and (0.35, 0.35, 0.35) in **Figure 3e**. A mirrored version of the trend was observed along the second half of the body diagonal (between the body center and opposite cube corner), with minima also existing at (0.65, 0.65, 0.65) and (0.85, 0.85, 0.85). These 16c sites can also be described as those in which oxygen is vacant relative to the fluorite structure, therefore these results support the experimental observation that the bixbyite crystal structure becomes more similar to fluorite upon oxygen incorporation.

To maintain charge neutrality upon oxidation, the incorporation of negatively charged oxygen interstitials must be followed by the creation of holes in the vanadium sublattice due to internal charge transfer from vanadium to oxygen. Holes in the vanadium sublattice can either be localized on a vanadium cation and give rise to p-type, or positively charged, polaronic conduction, or delocalized in the valence band, yielding a strongly correlated p-type metal. Given the small energy differences between vanadium oxidation states, localized charge compensation at vanadium lattice sites is

expected, in which two vanadium atoms oxidize for every oxygen interstitial present, as shown in Kröger-Vink notation below.

$$2V_V^X + \frac{1}{2}O_2(g) \rightarrow 2V_V^{\cdot} + O_i'' \qquad (1)$$

Indeed, X-ray photoelectron spectroscopy (XPS) confirms the presence of V^{4+} following air exposure. This is evident by a second peak contribution within the envelope of the V 2p doublet, which increases in intensity with annealing time at 125°C in air (**Figure 4**).

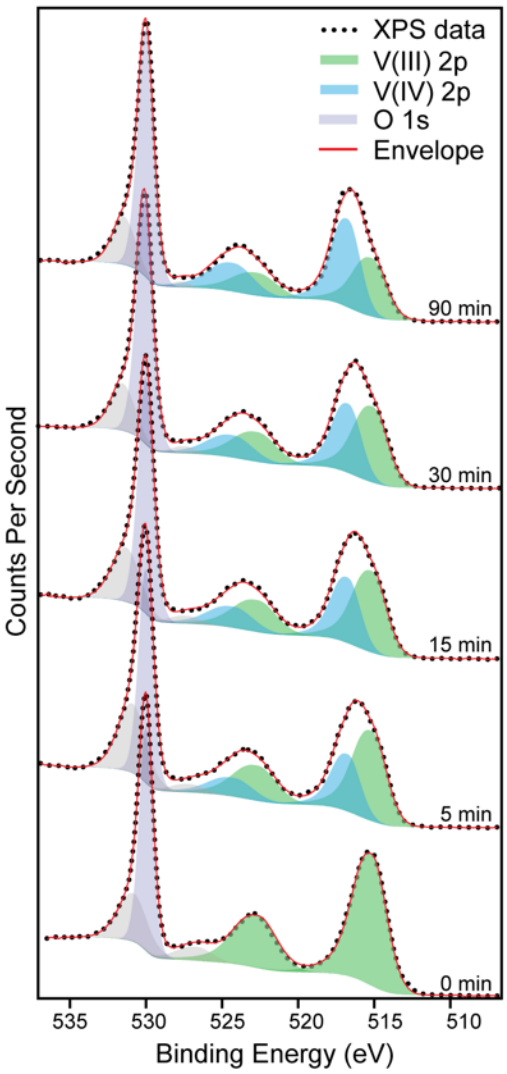

Figure 4. XPS scans of bixbyite films annealed in air at 125°C for 0, 5, 15, 30, and 90 minutes. The contribution of vanadium in the 3+ and 4+ oxidation states is indicated by the green and blue peaks, respectively.

The course of the bixbyite oxidation process that ultimately leads to phase transformation was followed in detail by carrying out *in situ* XRD experiments, like that shown in **Figure 2e**, at several temperatures. **Figure 5a** maps the position of the (222) diffraction peak from this data as a function of annealing time

at 100°C, 125°C, and 150°C. The rate of peak shift, and therefore volume expansion, increases with temperature up to the point of transformation, where the single peak at Q ≈2.3 $Å^{-1}$ splits into a peak and shoulder. No further structural changes are observed after this transition. **Figure 5b** shows weight gain, monitored by TGA, in bixbyite nanocrystals as a function of time under the same annealing conditions as *in situ* XRD. As temperature is increased, weight gain occurs at a faster rate. However the percentage of weight gain at transformation, determined from the maximum change in shoulder peak intensity (**Figure S3**) and marked with green circles in **Figure 5a & b**, is independent of annealing temperature. This suggests that the transformation is triggered once a critical oxidation level is reached. Taking the lattice as cubic up to the point of transformation and ascribing all weight gain to oxygen interstitial incorporation, *in situ* XRD and TGA data can be combined to track unit cell volume as a function of oxygen interstitial concentration. A non-linear trend is apparent with increasing expansion as oxidation proceeds (**Figure 5c**). The trend is consistent for annealing at 100°C and 125°C, while the data appear slightly shifted for 150°C annealing. We attribute this shift to partial oxidation during the ramp to 150°C, which would result in an underestimation of oxygen interstitial content. Based on the weight gain of about 1.8% at transformation, it can be reasoned that the bixbyite lattice can accommodate two oxygen interstitials per unit cell, after which the structure becomes unstable and transformation occurs. This result suggests that the oxidized phase has a stoichiometry between that of V_2O_3 and V_3O_5, the adjacent phase in the V-O phase diagram. However, efforts to identify its crystal structure were unsuccessful, as it indexes to no known vanadium oxide phase or fluorite derivative.

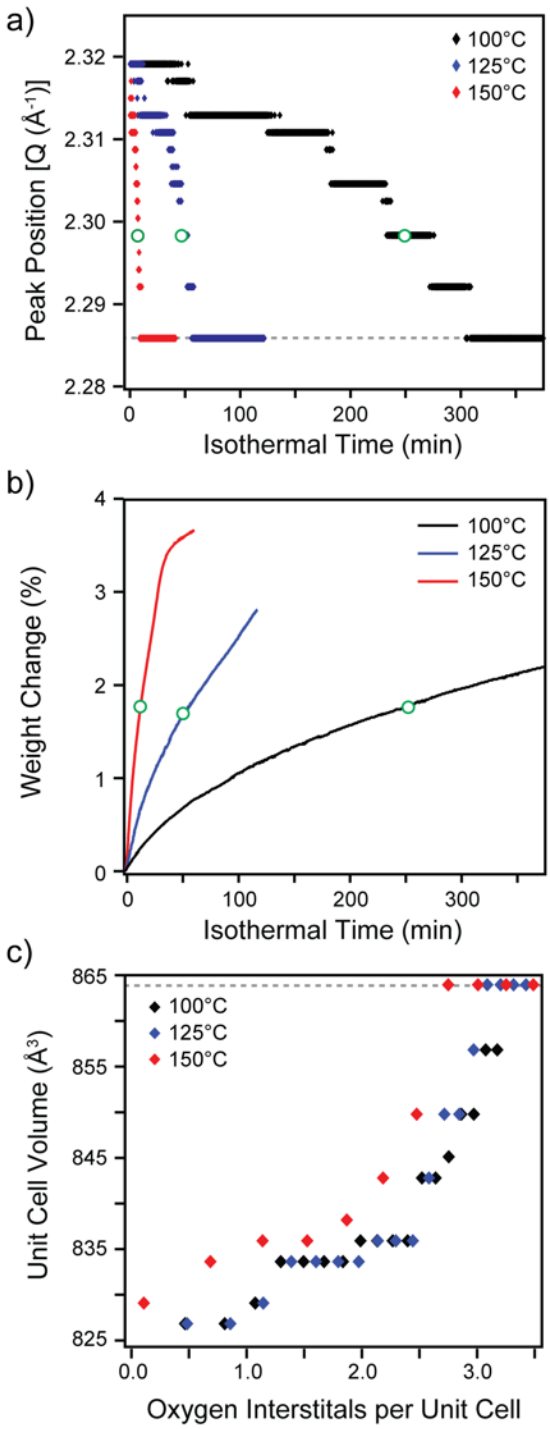

Figure 5. Kinetic progress of the oxidation of bixbyite V_2O_3 nanocrystals followed *in situ* during air annealing. a) (222) peak position from *in situ* XRD data and b) TGA scans for bixbyite nanocrystals annealed in air at 100°C (black), 125°C (blue), and 150°C (red). c) Volume expansion as a function of oxygen interstitial content calculated from data in a) and b). Green circles indicate time at which transformation to unknown phase occurs, as determined from maximum change in shoulder peak intensity.

The *in situ* data were also used to plot time to transformation as a function of annealing temperature, as shown in **Figure 6a**. An Arrhenius-type relation is apparent, in which transformation rate is related to temperature following:

$$k = Ae^{-E_a/RT} \qquad (2)$$

Where k is the reaction rate, A is an attempt frequency factor, E_a is the activation energy, R is the universal gas constant, and T is temperature. An activation energy and frequency factor of 98 kJ/mol (1.02 eV), and 3.1 x 10^9 s^{-1}, respectively, were extracted from the data. Activation energy is determined by the rate limiting step of the oxidation process, which may include oxygen adsorption, dissociation, intercalation, diffusion, and finally, structural transformation. Many of these potentially rate limiting processes are expected to be accelerated in materials with high surface area (*i.e.*, adsorption, dissociation, intercalation) or presenting short path lengths (*i.e.*, diffusion), so that the progression of the structure along an equilibrium pathway of progressive oxidation is greatly facilitated by the nanostructuring of the material. Oxidation happens quickly at the surface of the nanocrystal, as seen by the large concentration of charge compensating V^{4+} after only 5 minutes of annealing in **Figure 4**. Thus, it is unlikely that the processes occurring at the surface of the nanocrystal are rate limiting. Furthermore, the extracted activation energy is comparable to theoretical and experimental activation energies of oxygen diffusion in perovskite, fluorite, and bixbyite oxides, thereby suggesting that oxygen diffusion is the rate limiting step in the bixbyite oxidation process.[19–21] To support this hypothesis, the activation energy of oxygen diffusion was modeled using the climbing-image nudged elastic band method for DFT.[22,23] Neighboring minima along the body diagonal in the bixbyite unit cell, as shown in **Figure 3e**, were chosen as initial and final positions of the minimum energy pathway for oxygen migration. The resulting activation energy along this path was found to be 1.09 eV (**Figure 6b**). This result is in very good agreement with the activation energy extracted from experimental kinetics, thereby supporting the role of oxygen diffusion as the rate limiting step in the transformation process.

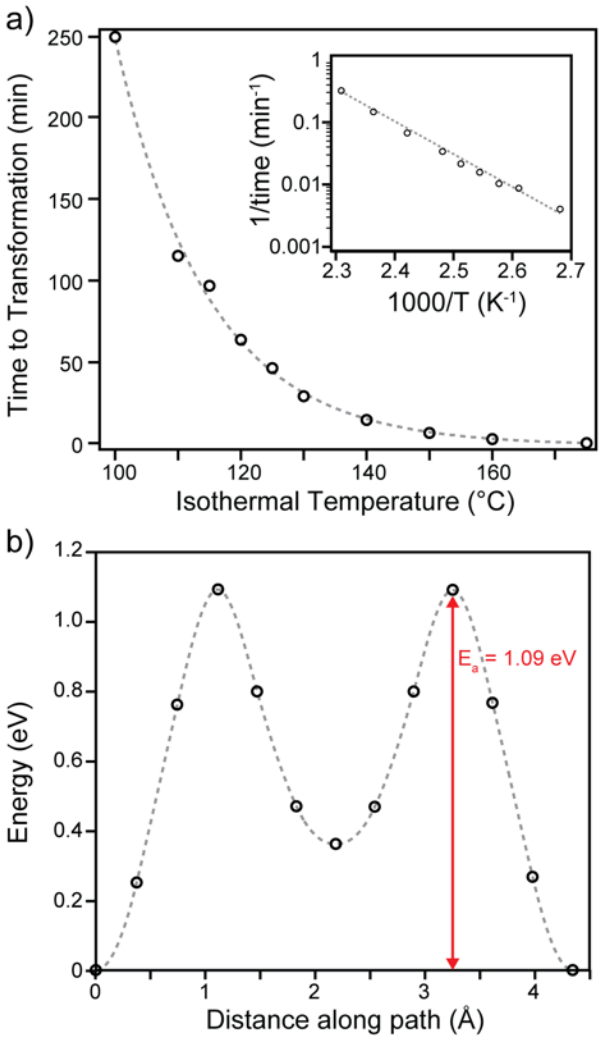

Figure 6. a) Time to transformation as a function of annealing temperature in air. Inset shows plot of 1000/T vs ln(1/t), yielding straight line which can be used to extract activation energy and frequency factor. b) Climbing-image nudged elastic band model of oxygen interstitial diffusion between neighboring 16c Wyckoff positions along the cell body diagonal.

Notably, the oxidation of bixbyite V_2O_3 can be reversed upon annealing in a mild reducing atmosphere, even if it has been allowed to progress past the phase transformation. **Figure 7a** shows *in situ* XRD scans from an already oxidized and transformed sample heated in helium to 325°C. The characteristic peak and shoulder of the unknown, oxidized phase merge into one peak, characteristic of the bixbyite phase, suggesting a phase transformation back to the stoichiometric phase. Indeed, the recovery of the bixbyite phase is confirm by *ex situ* XRD while TEM images show minimal changes to particle size and shape (**Figure S1**). Oxidized bixbyite was also heated under the same conditions as *in situ* XRD while weight loss was tracked by TGA. The starting weight of the sample corresponds to the weight after oxidation at 125°C, a continuation of the data in **Figure 5b**. Upon heating in inert gas, a weight loss is indeed observed, with the maximum rate of change in weight occurring at the same time and temperature as the rapid change in peak position, approximately 13 minutes and 310°C, respectively (**Figure S6**). However the final weight after reduction (~95 wt%) is less than the initial sample weight before

oxidation (100 wt%). This additional weight loss can be accounted for by the decomposition of the organic ligands bound to the surface of the nanocrystals, as evidenced by the 5 wt% loss in a pristine bixbyite sample heated under the same conditions (**Figure 7b**). The final weight of the oxidized sample is approximately equal to the final weight of the unoxidized sample, indicating that the weight gain due to oxygen insertion is completely reversed by annealing in nitrogen. Therefore, it is likely that the change in structure observed by *in situ* XRD is indeed due to reduction, wherein the phase transformation is reversed and oxygen interstitials are removed from the bixbyite lattice.

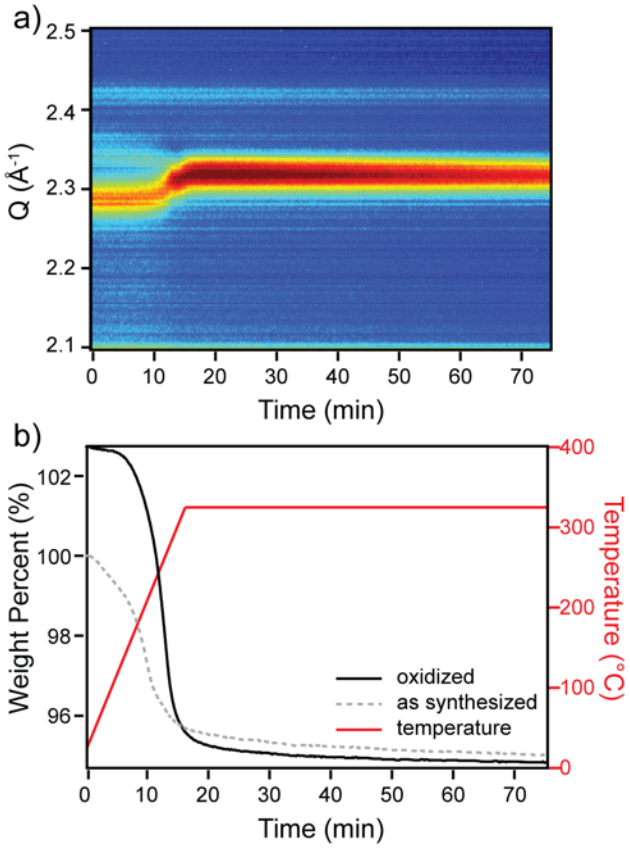

Figure 7- Reduction of oxidized bixbyite as observed by a) *in situ* XRD and b) TGA heated in inert gas following temperature profile in red. TGA data includes reduction of oxidized and as-synthesized bixbyite in order to account for ligand decomposition. The XRD peaks near Q=2.1 and 2.42 arise from the beryllium dome required for *in situ* inert gas annealing.

Such reversibility in the oxidation process requires not only kinetic facilitation by the nanoscale nature of the material, but favorable thermodynamics that allow the system to shift between thermodynamically favored states within the experimentally accessible range of environmental conditions. To probe the energetics of the defect formation process corresponding to oxygen insertion in bixbyite V_2O_3, DFT was used to evaluate the following equation for defect formation energy of a neutral cell[24]:

$$E_{defect} = E_{defective\ cell} - E_{perfect\ cell} - \sum_i n_i \mu_i \qquad (3)$$

Where μ_i is the chemical potential of species *i* added or removed and n_i is the number of species *i* added or removed (n_i <0 if removed, n_i >0 if added). For the case of an oxygen interstitial in the 80 atom unit cell of bixbyite, the equation becomes:

$$E_{O_i} = E_{V_{32}O_{49}} - E_{V_{32}O_{48}} - \mu_O \qquad (4)$$

The total energy of a stoichiometric, relaxed bixbyite cell was subtracted from the total energy of a cell with one additional interstitial oxygen initially at a position of (0.15, 0.15, 0.15) and relaxed to (0.141, 0.142. 0.143), as calculated by DFT. The lattice parameters were fixed to simulate the dilute limit. We note that the defect-defect distance is 9.414 Å and that only subtle elastic interactions between defects in periodic images is expected. As the chemical potential of oxygen depends on pressure and temperature, it is reported as a range of achievable values. The lower bound, or reducing limit, represents the chemical potential at which the dissociation of V_2O_3 into vanadium metal and oxygen gas becomes thermodynamically favorable, whereas at the upper bound, or oxidizing limit, the maximum chemical potential of oxygen considered is the total energy of oxygen in an isolated oxygen molecule. **Figure 8** shows the defect formation energy of an oxygen interstitial as a function of the chemical potential of oxygen.

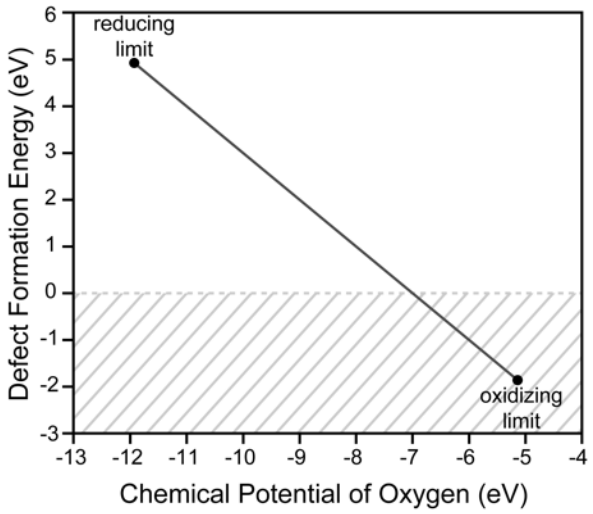

Figure 8- Defect formation energy of oxygen interstitial in bixbyite V_2O_3 calculated by DFT as a function of the chemical potential of oxygen for a range of experimentally accessible values. Dashed grey area indicates the region of negative defect formation energy.

The reversibility of the oxidation process observed experimentally can be understood from the calculated defect formation energy and its dependence on the chemical potential of oxygen. Under oxygen-rich conditions, oxygen has a higher chemical potential and the defect formation energy of an oxygen interstitial is negative. This result indicates that bixbyite is metastable with respect to a more oxidized phase under these conditions, which is consistent with our observation that bixbyite oxidizes spontaneously over time. Under oxygen-poor conditions (low chemical potential), the defect formation energy is positive, indicating that stoichiometric bixbyite is a stable host for oxygen interstitials. As the oxygen chemical potential decreases, either by reducing oxygen partial pressure or increasing

temperature, the defect formation energy increases, ultimately leading to a decrease in the equilibrium concentration of oxygen interstitials in bixbyite. This is consistent with our observation that oxygen interstitials are removed from the lattice upon heating under inert gas flow (low ppO2), as shown by XRD and TGA in **Figure 7**. Furthermore, distinct levels of reduction can be achieved by simply varying temperature while keeping partial pressure low and fixed (**Figure S4 & S5**). In this way, oxygen content can be controlled by altering either oxygen partial pressure, temperature, or both.

DISCUSSION

The ability to reversibly store and release oxygen in bixbyite V_2O_3 makes it an appealing candidate for use in oxygen storage applications. Oxidation occurs both rapidly and with minimal change in crystal structure below a concentration of approximately two oxygen interstitials per unit cell. However, the most remarkable feature of bixbyite's reversible oxidation process is the unusually low temperatures required for oxidation and reduction. For comparison, $HoMnO_3$, a hexagonal manganite material demonstrating oxidation at exceptionally low temperatures, requires an oxidation temperature of 190°C, while heating in pure O_2 gas, and a reduction temperature of 325°C.[25] Bixbyite V_2O_3 demonstrates nearly the same oxygen storage capacity at transformation (~1.8%) while operating at a lower temperature and ppO_2. In addition to aiding in the stabilization of the phase, the high surface to volume ratio in bixbyite NCs is expected to result in faster diffusion, and therefore faster switching kinetics, than in the bulk.[26] Furthermore, while most oxygen storage materials under investigation today contain rare earth elements, vanadium oxide is made up of earth-abundant elements.

To pave the way toward practical applications, further work is needed to improve cyclability of the oxidation and reduction processes. Initial tests show diminishing oxygen storage capacity upon cycling, leading to an eventual loss of bixbyite stabilization (**Figure S7**). This may be associated with the thermal decomposition of the binding organic ligands at the surface of the bixbyite nanocrystals which may alter surface energy and, therefore, stability of the phase. Repeated expansion and transformation induced by oxidation may also lead to degradation of the structure. Indeed, cycleability is improved when oxidation is not allowed to progress past the point of structural transformation. These problems may be mitigated by doping or alloying with elements that stabilize the metastable structure (as in yttrium-stabilized zirconia) or minimize defect-induced strain. The improved oxygen storage capacity and cyclability of zirconia-ceria solid solutions, compared to pure ceria, is an example of the latter. This improvement has been ascribed to the small size of the zirconium ion, which counteracts the strain associated with the formation of trivalent cerium during reduction.[27]

Lattice expansion in fluorite and defective fluorite-type oxides is not a new occurrence, but contrary to what is observed in V_2O_3, this tends to occur as a result of oxygen *vacancy* formation. Termed chemical expansion, this is a well-known phenomenon, due in part to the stresses this type of expansion can induce in energy conversion devices such as solid oxide fuel cells.[28] Charge compensating cation reduction, and the resulting increase in cationic radius, is the dominant mechanism leading to expansion in oxygen deficient fluorites and perovskites. Although relaxation near the vacancy causes some contraction, the effect is not as pronounced and therefore the net result is still expansion. Similarly, in bixbyite V_2O_3, two opposing influences on lattice parameter are expected. The presence of excess

oxygen is expected to favor expansion to accommodate lattice strain while the oxidation of vanadium, required for charge compensation, favors contraction. This is clear from the ionic radius of vanadium, which is 0.64 Å in the 3+ oxidation state and 0.58 Å in the 4+ state.[29] If change in cation size dominates the change in lattice constant, as it does in the case of chemical expansion observed in other fluorite-type structures, one might expect the net effect of these competing influences to favor contraction, however this is not observed. Instead, low concentrations of oxygen interstitials have very little effect on the lattice, as shown in **Figure 5c**, while larger concentrations result in expansion. We propose that the two competing mechanisms favoring expansion and contraction, strain accommodation and cation oxidation, respectively, balance and compensate each other at low oxidation levels. Upon further oxidation however, expansion due to accommodation of extra atoms in the lattice dominates. DFT calculations of unit cell volume as a function of oxygen interstitial content show a similar trend (**Figure S10**).

The reversible oxidation observed in bixbyite is not expected to occur in the other polymorphs of V_2O_3. Although vanadium is known for its ability to switch oxidation states, and could thereby compensate for the extra charge introduced by oxygen interstitials in any crystal phase, the corundum and monoclinic phases likely have insufficient space in the lattice to accommodate oxygen interstitials at reasonable formation energy. Corundum, for example, has a hexagonal close-packed oxygen sub-lattice that leaves little room for excess oxygen, quite unlike the inherently vacant sites in the bixbyite unit cell.[30] The calculated density of the bixbyite phase is 4.81 g/cm^3, as compared to the much higher densities of the corundum and monoclinic phases, which are 5.02 g/cm^3 and 4.98 g/cm^3, respectively.[2,31] Alternatively, other oxides with the bixbyite structure, such as indium oxide (In_2O_3), may be unable to easily compensate for the high levels of charge introduced by oxygen interstitials. As indium in the 3+ oxidation state has a stable [Kr]4d^{10} electron configuration, compensation by cation oxidation is highly unlikely. Furthermore, delocalized compensation, resulting in hole formation and p-type conductivity, is possible in semiconductors like In_2O_3 but never observed. Rather the formation of oxygen vacancies is known to be favorable in In_2O_3, leading to intrinsic n-type conductivity.[32]

It is therefore a combination of bixbyite's open structure and vanadium's ability to change oxidation state that hold the key to bixbyite V_2O_3's ability to accommodate large oxygen excesses under mild oxidation conditions. In this regard, its nanocrystalline morphology, which plays a role in stabilizing the less dense phase in addition to offering short diffusion paths, is clearly important. Lacking direct experimental data, however it is unclear whether this reversible process could occur effectively in bulk bixbyite.

CONCLUSIONS

Here we report reversible oxygen incorporation in metastable, bixbyite V_2O_3 nanocrystals. Oxygen interstitials fill the inherently vacant 16c positions in bixbyite, as suggested by Rietveld refinement results and supported by DFT calculations, making the structure more like that of fluorite. Increasing oxidation in bixbyite results in lattice distortion and expansion, eventually inducing a phase transformation to an unidentified phase. Combined XRD and TGA data reveals a non-linear chemical expansion, with minimal structural changes upon initial oxidation and rapid expansion up to a critical

oxidation level of 1.8 weight %, corresponding to about 3 oxygen interstitials per unit cell, at which point transformation occurs. The rate of transformation follows an Arrhenius relationship, which was used to extract the activation energy of the process from *in situ* XRD data. This activation energy is in good agreement with the calculated activation energy of oxygen diffusion determined by DFT, and therefore the oxidation process is reasoned to be diffusion limited. Finally, oxidation and transformation were shown to be reversible by annealing in inert gas at 325°C, with the structure reverting back to that of stoichiometric bixbyite and weight loss indicating the removal of interstitial oxygen from the lattice. The reversibility of the process can be understood by the dependence of defect formation energy on the chemical potential of oxygen, which can be controlled by varying oxygen partial pressure and temperature. This study motivates the continued effort in stabilizing a bulk form of bixbyite V_2O_3 in order to elucidate the influence of nanosize effects on reversible oxidation, as well as the further exploration of the strange and fascinating properties of this metastable oxide.

METHODS

Synthesis: In a typical synthesis using standard Schlenk line techniques, a 50 ml three-neck flask containing 0.265 g (1 mmol) vanadyl acetylacetonate (Strem Chemicals, 98%), 1.07 g (4 mmol) oleylamine (Sigma Aldrich, 70%), and 1.13 g (4 mmol) oleic acid (Sigma Aldrich, 98%) in 8 ml squalane (Sigma Aldrich, 99%) was degassed under vacuum at 110°C for 1 hour. The mixture was then heated, under nitrogen flow, to 370°C and held at this temperature for 1 hour. The nanocrystals were cleaned by repeated flocculation with isopropanol and redispersion in hexanes or toluene.

Transmission Electron Microscopy: Nanocrystals were drop cast onto a silicon nitride grid from a dilute suspension in hexanes and allowed to dry. Low resolution images were acquired using a JEOL-2010F microscope with a Schottky field emission gun operating at 200 kV and equipped with a CCD camera. After imaging, the grid was heated in air at 125°C for 2 hours to transform to oxidized phase, then imaged again.

X-Ray Diffraction: Nanocrystals in hexanes were drop cast onto silicon substrates to create films. These films were annealed in a Thermo Scientific Lindberg Blue M Mini-Mite tube furnace open to air at 125°C for 0, 10, 20, 30, 40, and 50 minutes, resulting in increasing levels of oxidation. XRD patterns of these films were collected at the Stanford Synchrotron Radiation Lightsource on beamline 2-1. The diffractometer, equipped with Huber 2-circle goniometer and a high-resolution crystal-analyzer detector, was operated at a 12 keV (λ = 1.033 Å) in reflection mode with the sample under helium flow. Scans were obtained between 2θ = 10° to 44° with a step size of 0.01° and time per step of 1 second. Scans were repeated 3 times then averaged. Rietveld refinement was performed on the data using the TOPAS 4.2 program.

In situ X-Ray Diffraction: *In situ* XRD was performed on beamline X20A at the National Synchrotron Light Source at Brookhaven National Laboratory. The diffractometer was operated in reflection mode, with a molybdenum sample heater, at an energy of 8.0645 keV (λ = 1.537 Å). Real time scans were collected using a 640-pixel linear detector centered at Q = 2.25 $Å^{-1}$ and positioned such that a Q range of 1.4 $Å^{-1}$ was surveyed during oxidation, corresponding to a resolution of 0.0022 $Å^{-1}$/pixel. Oxidation was

observed while the sample was open to air and heated to temperatures between 100 and 170°C. To observe the reduction of bixbyite, a beryllium dome was affixed to the stage and purged with helium. Samples were then heated to between 250 and 400°C. Integration time varied between 1 to 5 seconds, depending on the speed of transformation, and continued over the course of transformation.

Thermogravimetric Analysis: TGA was done using a Mettler Toledo TGA/DSC 1. To prepare the samples, several milligrams of clean nanocrystals in hexanes were drop cast into alumina crucibles and the solvent was allowed to evaporate. Experiments were run in nitrogen or air at a flow rate of 50 ml/min and temperature ramp rate of 20°C/min.

X-Ray Photoelectron Spectroscopy: XPS measurements were done using a Kratos Axis Ultra DLD X-ray photoelectron spectrometer with an aluminum X-ray source. The spectrometer was equipped with a series of chambers and a capsule, known collectively as ROX interface, which allow for air-free transfer from a glove box. XPS spectra were calibrated to the O1s peak at 530 eV following reference 33. High resolution spectra of the V $2p_{3/2}$, V $2p_{1/2}$, and O 1s peaks were acquired for samples annealed in air at 125°C, then analyzed using the CasaXPS software package. The peak at ~527 eV corresponds to a vanadium satellite while the peak at ~532 eV can be assigned to the oxygen-containing oleate ligands bound to the surface of the nanocrystals.[33,34]

Density Functional Theory: DFT[35,36] calculations were performed using the Vienna *Ab initio* Simulation Package (VASP) with a plane-wave basis set expanded up to a cutoff energy of 550 eV. [37,38] The projector augmented wave (PAW) method was used, treating 13 valence electrons for vanadium ($3s^2 3p^6 4s^2 3d^3$) and 6 valence electrons for oxygen ($2s^2 2p^4$). [39,40] Exchange-correlation effects were treated within the GGA+U formalism, employing the PBEsol functional[41] and a Hubbard U value of 2.2 eV applied to vanadium 3d states. For the 80-atom bixbyite unit cell, Brillouin zone integration was done on a Γ-centered 3x3x3 k-point mesh, while 4x6x6 and 6x6x2 k-meshes were used for the monoclinic and corundum phases, respectively. Spin-polarized calculations were done with antiferromagnetic ordering of vanadium 3d electrons for the monoclinic and bixbyite polymorphs. Atom positions were relaxed until residual forces became less than 0.01 eV/Å and the Birch Murnaghan equation was used to obtain the equilibrium lattice parameter.[42] The transition path for oxygen interstitial diffusion was explored without spin polarization using the climbing-image nudged elastic band method.[22,23] Atom positions within each image were relaxed until the forces became less than 0.03 eV/Å. Further details on DFT calculations are included in the SI.

ASSOCIATED CONTENT

Supporting Information is available free of charge on the ACS Publications website at

Examples of data analysis, further TGA and XRD data, parameter evaluation for DFT, structural modeling results.

ACKNOWLEDGEMENTS

The authors acknowledge Jean L. Jordan-Sweet, Badri Shyam, and Hugo Celio for assistance with XRD and XPS measurements, and Penghao Xiao, Sandra H. Skjærvø, Gerhard Olsen, and Tor Grande for helpful discussions. Use of the National Synchrotron Light Source, Brookhaven National Laboratory, was supported by the U.S. Department of Energy, Office of Science, Office of Basic Energy Sciences, under Contract No. DE-AC02-98CH10886. Use of the Stanford Synchrotron Radiation Lightsource, SLAC National Accelerator Laboratory, is supported by the U.S. Department of Energy, Office of Science, Office of Basic Energy Sciences under Contract No. DE-AC02-76SF00515. Computational resources were provided by NOTUR (The Norwegian Metacenter for Computational Science) through grant no. NN9264K. Additional support to DJM from the Welch Foundation (F-1848) is acknowledged.

This material is based upon work supported by the National Science Foundation Graduate Research Fellowship under Grant No. DGE 1106400. AB's extended research visit in Norway was supported by the NSF Graduate Research Opportunities Worldwide (GROW) Program in collaboration with the Research Council of Norway.

REFERENCES

(1) Morin, F. J. Oxides Which Show a Metal-to-Insulator Transition at the Neel Temperature. *Phys. Rev. Lett.* **1959**, *3*, 34–36.
(2) Dernier, P. D.; Marezio, M. Crystal Structure of the Low-Temperature Antiferromagnetic Phase of V_2O_3. *Phys. Rev. B* **1970**, *2*, 3771–3776.
(3) Moon, R. M. Antiferromagnetism in V_2O_3. *Phys. Rev. Lett.* **1970**, *25*, 527–529.
(4) Mott, N. F.; Zinamon, Z. The Metal-Nonmetal Transition. *Rep. Prog. Phys.* **1970**, *33*, 881.
(5) Weber, D.; Stork, A.; Nakhal, S.; Wessel, C.; Reimann, C.; Hermes, W.; Müller, A.; Ressler, T.; Pöttgen, R.; Bredow, T.; *et al.* Bixbyite-Type V_2O_3 —A Metastable Polymorph of Vanadium Sesquioxide. *Inorg. Chem.* **2011**, *50*, 6762–6766.
(6) Sarmadian, N.; Saniz, R.; Partoens, B.; Lamoen, D. Ab Initio Study of Shallow Acceptors in Bixbyite V_2O_3. *J. Appl. Phys.* **2015**, *117*, 015703.
(7) Xu, Y.; Zheng, L.; Wu, C.; Qi, F.; Xie, Y. New-Phased Metastable V_2O_3 Porous Urchinlike Micronanostructures: Facile Synthesis and Application in Aqueous Lithium Ion Batteries. *Chem. Eur. J.* **2011**, *17*, 384–391.
(8) Bergerud, A.; Buonsanti, R.; Jordan-Sweet, J. L.; Milliron, D. J. Synthesis and Phase Stability of Metastable Bixbyite V_2O_3 Colloidal Nanocrystals. *Chem. Mater.* **2013**, *25*, 3172–3179.
(9) Wyckoff, R. W. G. *Crystal Structures - Volume 2: Inorganic Compounds RXn, RnMX2, RnMX3*; Interscience Publishers, 1964.
(10) McHale, J. M.; Auroux, A.; Perrotta, A. J.; Navrotsky, A. Surface Energies and Thermodynamic Phase Stability in Nanocrystalline Aluminas. *Science* **1997**, *277*, 788–791.
(11) Zhang, H.; Banfield, J. F. Thermodynamic Analysis of Phase Stability of Nanocrystalline Titania. *J. Mater. Chem.* **1998**, *8*, 2073–2076.
(12) Dinega, D. P.; Bawendi, M. G. A Solution-Phase Chemical Approach to a New Crystal Structure of Cobalt. *Angew. Chem. Int. Edit.* **1999**, *38*, 1788–1791.
(13) Momma, K.; Izumi, F. *VESTA 3* for Three-Dimensional Visualization of Crystal, Volumetric and Morphology Data. *J. Appl. Crystallogr.* **2011**, *44*, 1272–1276.
(14) Wessel, C.; Reimann, C.; Müller, A.; Weber, D.; Lerch, M.; Ressler, T.; Bredow, T.; Dronskowski, R. Electronic Structure and Thermodynamics of V_2O_3 Polymorphs. *J. Comput. Chem.* **2012**, *33*, 2102–2107.

(15) Reimann, C.; Weber, D.; Lerch, M.; Bredow, T. Nonstoichiometry in Bixbyite-Type Vanadium Sesquioxide. *J. Phys. Chem. C* **2013**, *117*, 20164–20170.
(16) Jeen, H.; Choi, W. S.; Biegalski, M. D.; Folkman, C. M.; Tung, I.-C.; Fong, D. D.; Freeland, J. W.; Shin, D.; Ohta, H.; Chisholm, M. F.; *et al.* Reversible Redox Reactions in an Epitaxially Stabilized $SrCoO_x$ Oxygen Sponge. *Nat. Mater.* **2013**, *12*, 1057–1063.
(17) Hervieu, M.; Guesdon, A.; Bourgeois, J.; Elkaïm, E.; Poienar, M.; Damay, F.; Rouquette, J.; Maignan, A.; Martin, C. Oxygen Storage Capacity and Structural Flexibility of $LuFe_2O_{4+x}$ ($0 \le x \le 0.5$). *Nat. Mater.* **2014**, *13*, 74–80.
(18) Sugiura, M. Oxygen Storage Materials for Automotive Catalysts: Ceria-Zirconia Solid Solutions. *Catal. Surv. Asia* **2003**, *7*, 77–87.
(19) Manning, P. S.; Sirman, J. D.; Kilner, J. A. Oxygen Self-Diffusion and Surface Exchange Studies of Oxide Electrolytes Having the Fluorite Structure. *Solid State Ionics* **1996**, *93*, 125–132.
(20) Ágoston, P.; Albe, K. *Ab Initio* Modeling of Diffusion in Indium Oxide. *Phys. Rev. B* **2010**, *81*, 195205.
(21) Chroneos, A.; Vovk, R. V.; Goulatis, I. L.; Goulatis, L. I. Oxygen Transport in Perovskite and Related Oxides: A Brief Review. *J. Alloy. Compd.* **2010**, *494*, 190–195.
(22) Henkelman, G.; Uberuaga, B. P.; Jónsson, H. A Climbing Image Nudged Elastic Band Method for Finding Saddle Points and Minimum Energy Paths. *J. Chem. Phys.* **2000**, *113*, 9901–9904.
(23) Henkelman, G.; Jónsson, H. Improved Tangent Estimate in the Nudged Elastic Band Method for Finding Minimum Energy Paths and Saddle Points. *J. Chem. Phys.* **2000**, *113*, 9978–9985.
(24) Freysoldt, C.; Grabowski, B.; Hickel, T.; Neugebauer, J.; Kresse, G.; Janotti, A.; Van de Walle, C. G. First-Principles Calculations for Point Defects in Solids. *Rev. Mod. Phys.* **2014**, *86*, 253–305.
(25) Abughayada, C.; Dabrowski, B.; Kolesnik, S.; Brown, D. E.; Chmaissem, O. Characterization of Oxygen Storage and Structural Properties of Oxygen-Loaded Hexagonal $RMnO_{3+\delta}$ (R = Ho, Er, and Y). *Chem. Mater.* **2015**, *27*, 6259–6267.
(26) Grande, T.; Tolchard, J. R.; Selbach, S. M. Anisotropic Thermal and Chemical Expansion in Sr-Substituted $LaMnO_{3+\delta}$: Implications for Chemical Strain Relaxation. *Chem. Mater.* **2012**, *24*, 338–345.
(27) Mamontov, E.; Egami, T.; Brezny, R.; Koranne, M.; Tyagi, S. Lattice Defects and Oxygen Storage Capacity of Nanocrystalline Ceria and Ceria-Zirconia. *J. Phys. Chem. B* **2000**, *104*, 11110–11116.
(28) Bishop, S. R.; Marrocchelli, D.; Chatzichristodoulou, C.; Perry, N. H.; Mogensen, M. B.; Tuller, H. L.; Wachsman, E. D. Chemical Expansion: Implications for Electrochemical Energy Storage and Conversion Devices. *Annu. Rev. Mater. Res.* **2014**, *44*, 205–239.
(29) Shannon, R. D. Revised Effective Ionic Radii and Systematic Studies of Interatomic Distances in Halides and Chalcogenides. *Acta Crystallogr. A* **1976**, *32*, 751–767.
(30) Sokol, A. A.; Walsh, A.; Catlow, C. R. A. Oxygen Interstitial Structures in Close-Packed Metal Oxides. *Chem. Phys. Lett.* **2010**, *492*, 44–48.
(31) Dernier, P. D. The Crystal Structure of V_2O_3 and $(V_{0.962}Cr_{0.0382})_2O_3$ near the Metal-Insulator Transition. *J. Phys. Chem. Solids* **1970**, *31*, 2569–2575.
(32) Lany, S.; Zunger, A. Dopability, Intrinsic Conductivity, and Nonstoichiometry of Transparent Conducting Oxides. *Phys. Rev. Lett.* **2007**, *98*, 045501.
(33) Silversmit, G.; Depla, D.; Poelman, H.; Marin, G. B.; De Gryse, R. Determination of the V2p XPS Binding Energies for Different Vanadium Oxidation States (V^{5+} to V^{0+}). *J. Electron Spectrosc.* **2004**, *135*, 167–175.
(34) Wilson, D.; Langell, M. A. XPS Analysis of Oleylamine/Oleic Acid Capped Fe_3O_4 Nanoparticles as a Function of Temperature. *Appl. Surf. Sci.* **2014**, *303*, 6–13.
(35) Hohenberg, P.; Kohn, W. Inhomogeneous Electron Gas. *Phys. Rev.* **1964**, *136*, B864–B871.

(36) Kohn, W.; Sham, L. J. Self-Consistent Equations Including Exchange and Correlation Effects. *Phys. Rev.* **1965**, *140*, A1133–A1138.
(37) Kresse, G.; Furthmüller, J. Efficiency of Ab-Initio Total Energy Calculations for Metals and Semiconductors Using a Plane-Wave Basis Set. *Comp.Mater. Sci.* **1996**, *6*, 15–50.
(38) Kresse, G.; Hafner, J. *Ab Initio* Molecular Dynamics for Liquid Metals. *Phys. Rev. B* **1993**, *47*, 558–561.
(39) Kresse, G.; Joubert, D. From Ultrasoft Pseudopotentials to the Projector Augmented-Wave Method. *Phys. Rev. B* **1999**, *59*, 1758–1775.
(40) Blöchl, P. E. Projector Augmented-Wave Method. *Phys. Rev. B* **1994**, *50*, 17953–17979.
(41) Perdew, J. P.; Ruzsinszky, A.; Csonka, G. I.; Vydrov, O. A.; Scuseria, G. E.; Constantin, L. A.; Zhou, X.; Burke, K. Restoring the Density-Gradient Expansion for Exchange in Solids and Surfaces. *Phys. Rev. Lett.* **2008**, *100*.
(42) Birch, F. Finite Elastic Strain of Cubic Crystals. *Phys. Rev.* **1947**, *71*, 809–824.